NJC

ROYAL SOCIETY OF CHEMISTRY

PAPER

View Article Online
View Journal | View Issue

Cite this: *New J. Chem.*, 2021, **45**, 7705

Fluorescence imaging of surface-versatile latent fingerprints at the second and third level using double ESIPT-based AIE fluorophore†

Manzoor Ahmad, [a] Gulshan Kumar, [b] Vijay Luxami, [b] Satwinderjeet Kaur, [c] Prabhpreet Singh [a] and Subodh Kumar *[a]

Received 9th February 2021,
Accepted 26th March 2021

DOI: 10.1039/d1nj00678a

rsc.li/njc

Latent fingerprints (LFPs) identification is of paramount importance for national security and criminal investigations. We designed and synthesized fluorescent organic molecule **HPBI** for the rapid fluorescence imaging of latent fingerprints on various surfaces such as aluminium foil, currency paper, brick, and glass, which did not require any post treatment. The **HPBI** exhibits a combination of ESIPT and AIE properties and forms green fluorescent nano-aggregates in $CH_3CN–H_2O$ (1 : 1) mixture, as evaluated by DFT, SEM, TEM, and fluorescent microscopic studies. Spraying the solution of spherical **HPBI** nanoaggregates (50–100 nm size) on various surfaces resulted in fluorescence display of LFPs in <2 minutes. LFPs clearly revealed level-2 (ridge ending, islands, bifurcation) and level-3 (ridges path deviation, edge contours, sweat pores) details with high contrast and no background interference. The relocation of fluorescent fingerprints on cello tape provides an efficient and clean method for carrying fingerprints to the forensic laboratory.

1. Introduction

Fingertips have a characteristic fluted skin with raised papillary ridges and shallow furrows.[1] They consist of a mixture of natural secretions (sebum, lipids, sweat, *etc.*) and impurities from the environment.[2] When they come in contact with a surface, their ridge pattern is almost duplicated, transferring secretions to the surface.[3] The arrangement of papillary ridges varies not only from individual to individual but also from finger to finger and remains unchanged topologically from birth.[4] For personal identification and criminal investigations, fingerprints have become a well-established signature since the 19th century.[5] Papillary ridges being complex, unique, and stable are still used as the best reference in forensic science.[6] Though the advent of DNA technology has aided in robust identification, still LFPs play an important role in personal individualization and identification.[7] LFPs left on the surface remain invisible to the naked eye and over time, a number of methods have been developed for their visualization[7,8] such as chemical staining, nanoparticle reagents,[9,10] spectroscopic analysis,[11] nucleic acid recognition reagents,[12–14] powder dusting,[15] conjugated polyelectrolytes[16–18] aggregation-induced fluorescence,[19–24] electrochemical/electro-chemiluminescence methods,[25–27] and multi-metal deposition.[28,29] The commercially available methods for LFPs development and visualization not only suffer due to the background interference but are also associated with serious drawbacks such as cyanoacrylate fuming,[30] which can be used only for smooth surfaces and requires a large amount of time. Ninhydrin and 1,8-diazafluoren-9-one spraying can be used only for rough surfaces and require heating. The powder dusting technique, which is currently used in forensic investigations, faces multiple challenges such as low contrast due to non-fluorescence powder and requires brushing, which could damage LFPs. Fluorescent probes provide better visualization and efforts have been made by researchers for the development of luminous LFPs using AIE[19–24]-based probes and conjugated polyelectrolytes.[16–18] In recent times, aggregation-induced emission (AIE) properties have been explored for the better visualization of LFPs using AIE-active molecules.

We have designed and synthesized an AIE-active molecule **HPBI** for the rapid development and fluorescence imaging of latent fingerprints on multiple surfaces such as aluminium foil, currency paper, brick, and glass. **HPBI** exhibits a combination of ESIPT and AIE properties on increasing the fraction of water to the solution of **HPBI** in acetonitrile and gives maximum green fluorescence at 545 nm in 1 : 1 acetonitrile–water mixture due to the formation of the nano-aggregates of 50–100 nm size. On spraying the nano-aggregates of **HPBI** on various surfaces,

[a] *Department of Chemistry, Guru Nanak Dev University, Amritsar – 143005, India. E-mail: subodh_gndu@yahoo.co.in*
[b] *School of Chemistry and Biochemistry, Thapar Institute of Engineering and Technology, Patiala-147004, India*
[c] *Department of Botanical and Environment Science, Guru Nanak Dev University, Amritsar 143005, India*

† Electronic supplementary information (ESI) available. See DOI: 10.1039/d1nj00678a

ridges were filled with fluorescent nano-aggregates due to hydrophobic and electrostatic interactions between the nano-aggregates and components of fingerprint ridges in <2 minutes. LFPs clearly reveal level-2 details ncluding ridge ending, islands, and bifurcation, and level-3 details such as ridges path deviation, edge contours, and sweat pores with high contrast and no background interference. Besides this, fluorescent LFPs were relocated on cello tape without any abrasion or loss of information.

2. Experimental

2.1 Materials and Instruments

All chemicals were purchased from SpectroChem and used as received. TLC was performed on aluminium sheets coated with silica gel 60F254 (Merk, Darmstadt). Deionized water was obtained from ULTRA UV/UF Rions Lab Water system Ultra 370 series. NMR spectra were recorded on a JEOL 400 MHz NMR spectrometer with TMS as the internal standard. Abbreviations used for the splitting pattern are s = singlet, d = doublet, t = triplet, q = quartet, and m = multiplet. Mass spectrum was obtained from mass Bruker micro TOF QII mass spectrometer. The absorption spectra were recorded on a SHIMADZU-2450 spectrometer equipped with a Peltier system as the temperature controller. Quartz cuvettes of 1 cm path length were used for the absorbance and fluorescence measurements. Fluorescence spectra were recorded on a Fluorolog Horiba scientific model: FL-1039A/40A using slit widths (excitation = 1 nm and emission = 1 nm) and an excitation wavelength of 350 nm, unless otherwise stated. DLS measurements were performed at 25.0 + 0.1 °C using a Zetasizer nano ZS instrument. SEM was performed on a ZEISS SUPRATM 55 operating at an acceleration voltage of 10 kV with a tungsten filament as the electron source. The TEM images were obtained with a JEOL JEM-2100 electron microscope operating at an acceleration voltage of 200 kV. Fluorescence microscopic images were captured by a Nikon Eclipse Ts2 microscope using 365 nm light and 4× as the objective lens.

2.2 Synthesis of aldehyde 2[31]

2-(2-Hydroxyphenyl)benzothiazole[32] (**1**) (9.8 mM, 3 g) was dissolved in TFA (25 mL) in RBF (250 mL) at RT. Hexamine (12 mM, 1.7 g) was added and the reaction mixture was stirred at 60 °C for 36 h, during which **1** was completely consumed (TLC). The reaction mixture was allowed to cool down to RT, treated with HCl (4 N, 20 mL), and was poured into crushed ice. The solid that separated was filtered and washed with water. The crude solid was purified by column chromatography using hexane-ethyl acetate (5 : 1) as the eluent to obtain light green solid compound **2**, 2.4 g, 73%. ^{1}H NMR (DMSO-d_6, 400 MHz) ppm: δ 7.52 (t, J = 7.6 Hz, 1H, ArH), 7.61 (t, J = 8Hz, 1H, ArH), 8.04 (d, J = 3.2 Hz, 1H, ArH), 8.15 (d, J = 8 Hz, 1H, ArH), 8.23 (d, J = 8 Hz, 1H, ArH), 8.56 (d, 3.2 Hz, 1H, ArH), 10.27 (s, 1H, CHO); ^{13}C NMR (DMSO-d_6, 100 MHz) ppm: δ102.7, 122.0, 122.2, 124.4, 126.3, 126.6, 127.2, 133.2, 135.8, 151.8, 163.7, 190.8. HRMS for $C_{14}H_8BrNO_2S$ found at 333.9392, 335.9382 (1 : 1), expected for M^+ + 1 at 333.9537, 333.9531 (1 : 1).

2.3 Synthesis of HPBI

Aldehyde **2** (0.5 mM, 167 mg) was dissolved in a mixture of ethanol (10 mL) and THF (5 mL) in a 50 mL RBF. Compound **3** (0.5 mM, 154.8 mg) and acetic acid (100 μL) were added and the reaction mixture was refluxed for 4 h. The solvent was removed under vacuum and the residue was crystallized from ethanol to get **HPBI**, a bright red solid, yield 83% (260 mg). mp. 248 °C, R_f = 0.54 (2 : 8 ethyl acetate–hexane), ^{1}H NMR (DMSO-d_6, 400 MHz) ppm: δ 3.39 (6H, s, 2 × NCH_3), 7.15–7.38 (m, 10H, ArH), 7.40 (t, J = 7.6Hz, 1H, ArH), 7.52 (d, J = 7.6Hz, 1H, ArH) 7.55 (d, J = 2.4 Hz, 1H, ArH), 7.96 (d, J = 8Hz, 1H, ArH), 8.10 (d, J = 7.6 Hz, 1H, ArH), 8.63 (d, J = 2.4 Hz, 1H, ArH), 9.96 (s, 1H, imine H); ^{13}C NMR ($CDCl_3$, 100 MHz): δ 41.6, 110.8, 121.3, 122.8, 124.8, 126.1, 127.9, 128.6, 129.0, 129.1, 129.4, 129.9, 132.9, 134.6, 137.3, 151.9, 154.3, 157.6, 158.7, 159.4. HRMS for $C_{32}H_{24}BrN_5O_2S$ found 622.0939, 624.0923 (1 : 1); expected for M^+ + 1 at 622.0912, 624.0892 (1 : 1).

2.4 Computational studies

Ground state (S_0) geometry optimizations and frequency calculations were carried out using density functional theory (DFT)/B3LYP and the TZVP level of the basis set using Gaussian 16B. The excitation and emission energy calculations were performed using time-dependent DFT (TDDFT) using the same level of theory. The experimental environmental effects were considered using the IEF-PCM solvent model for acetonitrile. The stability of all the structures was confirmed by the absence of imaginary frequency. Further, potential energy curves (PECs) of proton transfer at the ground state (S_0) and the first excited state (S_1) were calculated at the same level using relaxed scans around the OHN intra-molecular hydrogen bonding.

2.5 Preparation of solutions

A stock solution of **HPBI** (4×10^{-4} M) was prepared in acetonitrile by the direct weighing of **HPBI**. The solutions of **HPBI** (5 μM) in binary mixtures of CH_3CN-water were prepared by adding 125 μL of the stock solution in a measuring flask (10 mL) and diluting it with the appropriate binary mixture of CH_3CN–water. For LFP studies, the solution of **HPBI** (50 μM) was prepared in CH_3CN–water (1 : 1).

2.6 Quantum yield determination

Fluorescence quantum yields (Φ_s) of **HPBI** solutions were determined using quinine sulfate (1 μM, 0.1 M $HClO_4$), Φ = 0.54, excitation wavelength 350 nm and fluorescein (1 μM, 0.1 N NaOH in water), Φ = 0.89, excitation wavelength 430 nm, as the reference compounds. The following equation

$$\Phi_s = \Phi_r(A_rF_s/A_sF_r)(\eta_s{}^2/\eta_r{}^2)$$

was used for calculating the quantum yields of various samples, where r and s represent the reference and the sample, respectively; Φ denotes the quantum yield; A signifies the absorbance; F denotes the relative integrated fluorescence; and η implies the refractive index of the medium.

2.7 UV-Vis and fluorescence studies

For recording the absorbance and fluorescence spectra of the desired solutions, 3 mL solution was poured into a cuvette with a path length of 1 cm and was kept for 2 minutes to attain 25 °C temperature before recording the spectrum. All fluorescence and absorption scans were saved as ACS II files, which were further processed in Microsoft Excel to produce the graphs.

2.8 FE-SEM and TEM images

Thin films for recording the SEM and TEM images were prepared by the drop casting method. For recording the SEM images, 10 μL solution of **HPBI** (5 and 50 μM) in 1 : 1 CH_3CN–water was put on a glass surface and was allowed to dry at 25 ± 1 °C in a thermostat. Once the thin film was formed, it was gold-coated before recording the FE-SEM image. For recording the TEM images, 1 μL solution of **HPBI** (50 μM) in 1 : 1 CH_3 CN–water was put on a copper grid and allowed to dry at 25 ± 1 °C. This thin film on the copper grid was used for recording the TEM image.

2.9 Dynamic light Scattering (DLS) studies

The stock solution of **HPBI** in CH_3CN and solvents such as CH_3CN and water were filtered through a membrane (0.2 micron) to remove any suspended particles. The solutions in desired solvents were prepared by putting **HPBI** (125 μL) and the appropriate solvents in a measuring flask (10 mL). Each solution was kept for at least 2 h before recording its DLS. 3 mL solution was placed in a cuvette of 1 cm path length and allowed to stand for 3 min before recording the DLS.

2.10 Development and visualization of latent fingerprints

The latent fingerprints (LFPs) were developed on surfaces such as aluminium foil, steel plate, marble sheet, coin, and paper currency. The donor (32–33 years old male) pressed the thumb on the desired surface softly. It is humans' natural instinct to involuntarily touching their face[33–35] continuously; thus, before depositing fingerprints on various surfaces, the fingertips were not restricted to touch facial features. The fingerprint marks on various surfaces were treated with 0.5 mL to 1 mL solution of **HPBI** (50 μM, CH_3CN–water 1 : 1) for less than a minute's time and the surface was washed with water and blown with air to dry it. Photographs of these fluorescent LFPs were captured under illumination of 365 nm light using a Canon 77D camera. The images captured were used as such or were only cropped without any color and brightness manipulation. For lifting the LFPs, the cello-tape (2 cm wide) was placed carefully on the LFP and was removed after 2 minutes.

3. Results and discussion

3.1 Synthesis of HPBI

The scheme for the synthesis of the probe **HPBI** is given in Scheme 1. The reaction of 2-aminothiophenol with 4-bromo-salicylaldehyde in ethanol in the presence of sodium bisulphite ($NaHSO_3$) gave 2-(2-hydroxy-4-bromophenyl)-benzothiazole (**1**) in

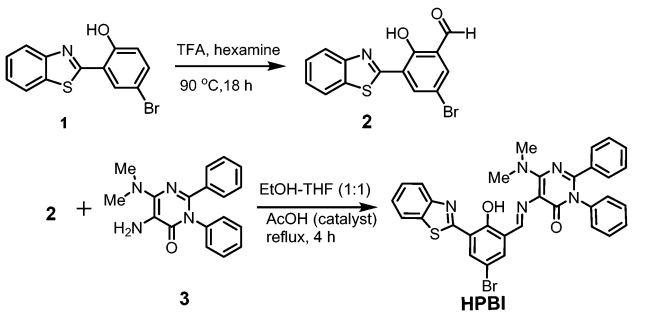

Scheme 1 Synthesis of probe **HPBI**.

78% yield. The formulation of **1** with hexamethylenetetramine in TFA gave the respective formyl derivative **2** in 73% yield. The condensation of aldehyde **2** with aromatic amine **3** in ethanol–THF (1 : 1) gave the probe **HPBI** in 83% yield. The ^{1}H NMR spectrum of **HPBI** showed the presence of dimethylamino 6H singlet at δ 3.39, hydroxyphenyl moiety two 1H doublets at δ 7.55 and δ 8.63 with 2.4 Hz coupling constant and imine 1H singlet at δ 9.96 along with other desirable signals for protons and confirmed the formation of **HPBI**. In its high-resolution mass spectrum, the presence of the parent ion peak at 622.0939, 624.0923 (1 : 1) further conspicuously confirmed the formation of **HPBI**. The formation of intermediate derivative **2** was also confirmed by the spectral data such as ^{1}H and ^{13}C NMR, and HRMS (ESI,† Fig. S1–S6).

3.2 Computational studies: structure optimization and tautomer investigations

The probe **HPBI** may be present in two enol forms, namely, **HPBI-1E** and **HPBI-2E**, and so can follow double ESIPT process to achieve two keto forms, **HPBI-1K** and **HPBI-2K**, on excitation. Therefore, ground state geometry optimization for **HPBI** was performed for enol conformations **HPBI-1E** and **HPBI-2E** and keto forms **HPBI-1K** and **HPBI-2K** (Fig. 1, ESI† Fig. S7) at DFT/B3LYP/6-31+G**. Both enol conformations are stabilized by OH···N hydrogen bonding but configuration **HPBI-1E** is more stable by 1.906 kcal mol^{-1} than **HPBI-2E** (Scheme 2). The absence of an imaginary frequency confirmed their stable geometry.

Further, to examine the nature of the excited state structures, the frontier molecular orbitals (FMOs) for the enol forms **HPBI-1E** and **HPBI-2E** were calculated. The calculated electronic excitations and relative oscillation strengths predict that the transition S_0 to S_1 occurs from the highest occupied molecular orbital (HOMO) to the lowest occupied molecular orbital (LUMO) with a contribution of 95% for **HPBI-1E** and 98% for **HPBI-2E** (Fig. 1). For **HPBI-1E**, HOMO to LUMO transition is π–π* electron transfer with a low degree of charge transfer from the $N(Me)_2$ unit to the benzothiazole moiety and the Schiff base core. The electron density in this transition decreases at the phenol moiety and increases at the imine nitrogen. It is also noteworthy that the contribution of hydroxy oxygen atom dropped from 2.55% to 0.07%, while that of imine nitrogen atom increased from 2.95% to 10.05%. On the other hand, for conformer **HPBI-2E**, the contribution of oxygen atom dropped

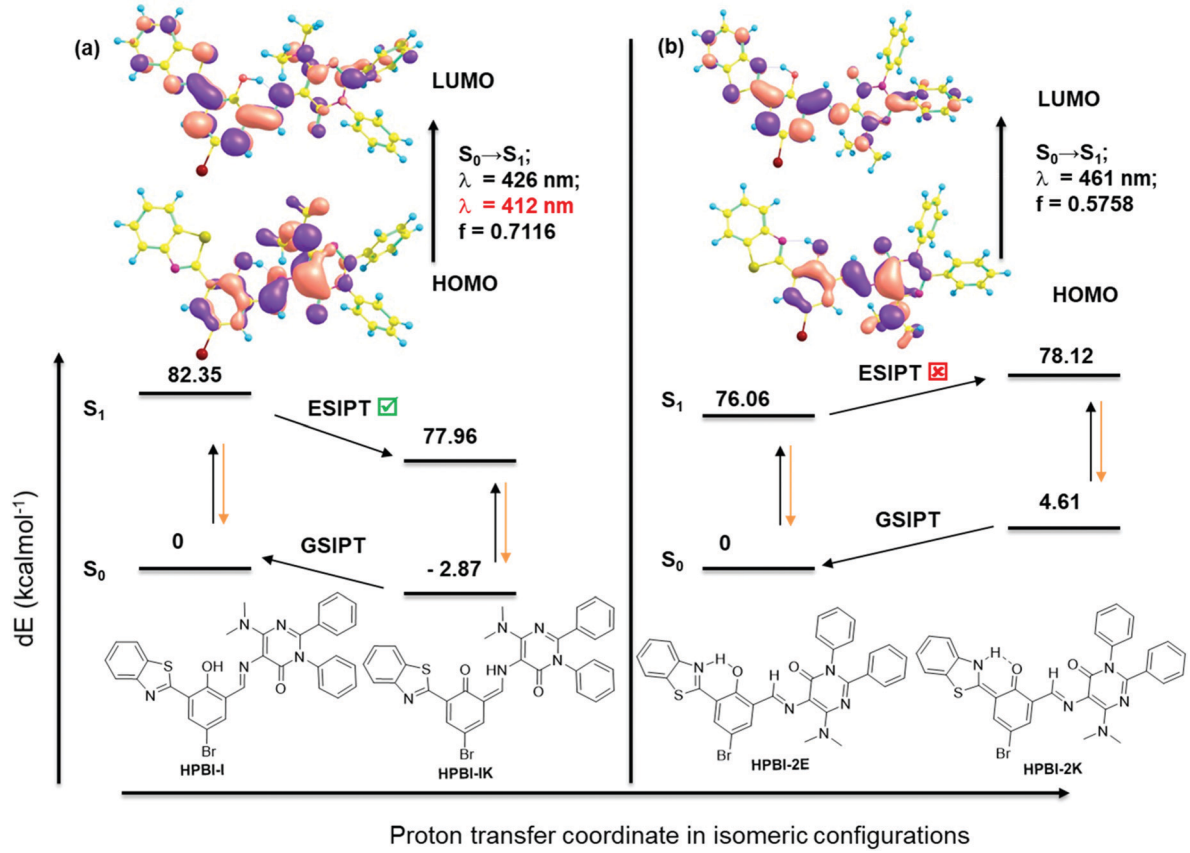

Fig. 1 The ESIPT process for two conformers of **HPBI**.

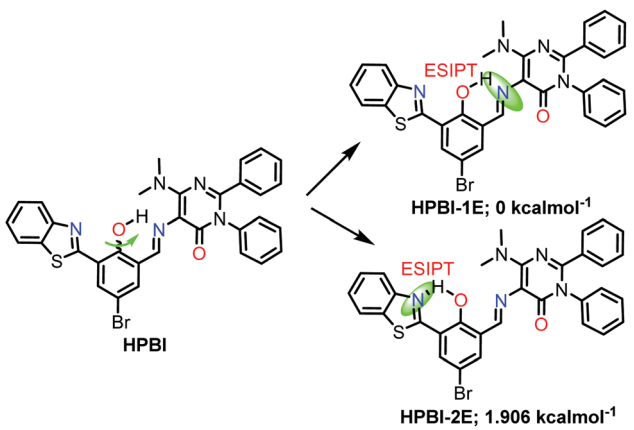

Scheme 2 Possible conformations of **HPBI** due to rotational flexibility at the phenolic center along with their relative energies.

from 2.61% to 0.006%, while for the benzothiazole nitrogen atom, it increased from 0.06% to 2.74%. Therefore, the excited state proton transfer dynamics could be more efficient in **HPBI-1E** than in **HPBI-2E**.

The photo-excitation of a molecule alters the electronic distribution influenced by the properties of the excited state. The structure optimization of the excited states of **HPBI-1E** and **HPBI-2E** and their tautomeric forms **HPBI-1K** and **HPBI-2K** further provides the insight for the relative efficiency of this double ESIPT process. It has been found that in the excited state, the tautomer **HPBI-1K** is lower in energy than the excited state of **HPBI-1E**, whereas the reverse is true in the case of **HPBI-2**. Thus, ESIPT could be more efficient in conformer **HPBI-1** than in **HPBI-2**. The predicted emission profiles for **HPBI-1K** is in close coherence with the observed emission maxima at 557 nm (CH_3CN–water 1 : 1, predicted 547 nm) and 593 nm (water, predicted 620 nm). The experimentally found higher quantum yield for the 557 nm emission band than for the 593 nm emission band is in consonance with the calculated results.

3.3 UV-Vis and fluorescence behavior of HPBI in CH_3CN–water binary mixtures

The UV-Vis and fluorescence spectra were recorded for 5 μM solutions of **HPBI**. The electronic spectrum of **HPBI** in CH_3CN displayed low energy absorption band at 412 nm and high energy band at 350 nm. On increasing the amount of f_w from 0% to 40%, the absorption gradually decreased with a shift in the maxima to longer wavelength and finally in solution with f_w 40%, it appeared at 435 nm with a red shift of ~23 nm. Based on Kasha's theory,[36] the red shift in the absorption band could be assigned to the formation of J-aggregates. Interestingly, a further increase in f_w from 50% to 90% showed no change in

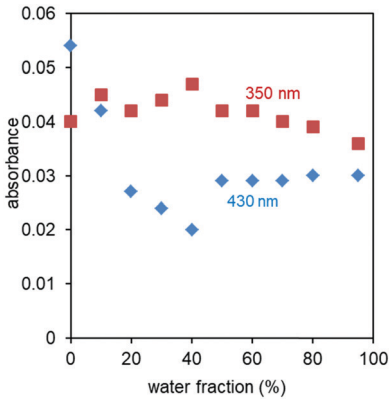

Fig. 2 Plot of absorbance at 430 nm and 350 nm *vs.* f_{water}.

the position of this low energy maximum (ESI,† Fig. S8). The plot of absorbance at 430 nm and 350 nm *vs.* f_w reveals that on increasing f_w from 0 to 40%, the value of absorption at 430 nm gradually decreases and is remains constant between 50 and 90% but at 350 nm, on increasing f_w from 0 to 40%, the absorbance increases and after that it decreases. Therefore, the two absorption bands at 430 nm and 350 nm behave differently (Fig. 2).

As the absorption spectra of the solutions of **HPBI** in various binary mixtures displayed two absorption bands at 350 nm and 412–430 nm, the fluorescence efficiency of these absorption bands was first evaluated. For these evaluations, the solutions of **HPBI** were prepared in CH_3CN, CH_3CN–water (1 : 1), and CH_3CN–water (1 : 9), and their fluorescence spectra were recorded using excitation wavelengths 350 nm and 430 nm. The quantum yields for these solutions were determined using quinine sulphate (for 350 nm excitation wavelength) and fluorescein (for 430 nm excitation wavelength) as the reference compounds. It has been observed that the higher energy absorption band at 350 nm gives fluorescence with higher fluorescence quantum yields in comparison to that calculated using 430 nm as the excitation wavelength (Table S1, ESI†). Therefore, all the fluorescence spectra were further recorded using 350 nm as the excitation wavelength.

The fluorescence spectra of **HPBI** (5 μM) in binary CH_3CN–H_2O solutions with increasing fraction of water were recorded using λ_{ex} = 350 nm. The solution of **HPBI** in CH_3CN displayed emission spectrum with λ_{em} at 555 nm. On increasing the f_w from 0 to 10% and then to 20%, the emission maxima blue shifted to 549 nm and 541 nm, respectively (Fig. 3A). On increasing f_w from 0 to 50%, the fluorescence intensity increased by nearly 150% and the solution became bright green fluorescent under illumination of 365 nm light. The solution of **HPBI** with f_w 30–50% revealed only a small change (<10%) in their fluorescence intensity. Significantly, on further increasing f_w to 60% and 70%, the fluorescence intensity decreased sharply (Fig. 3B and C). The solution of **HPBI** in CH_3CN–H_2O (20 : 80) and (10 : 90) solvents displayed two distinct emission bands at 542 nm and 590 nm, respectively (Fig. 3B). Finally, **HPBI** in H_2O gave emission with maxima at only 593 nm and the solution appeared fluorescent orange (Fig. 3D) under illumination of 365 nm light.

Further, to rationalize the effect of concentration of **HPBI** on the fluorescence intensity, the solutions of **HPBI** with concentrations 5–70 μM were prepared in the CH_3CN–H_2O (1 : 1) mixture. The plot of the fluorescence intensity against **HPBI** concentration reveals that fluorescence intensity increases linearly between 5–50 μM concentration of **HPBI** and then gradually increases slowly but does not lead to the quenching of fluorescence (ESI,† Fig. S9). There was a 4.5-fold increase in the

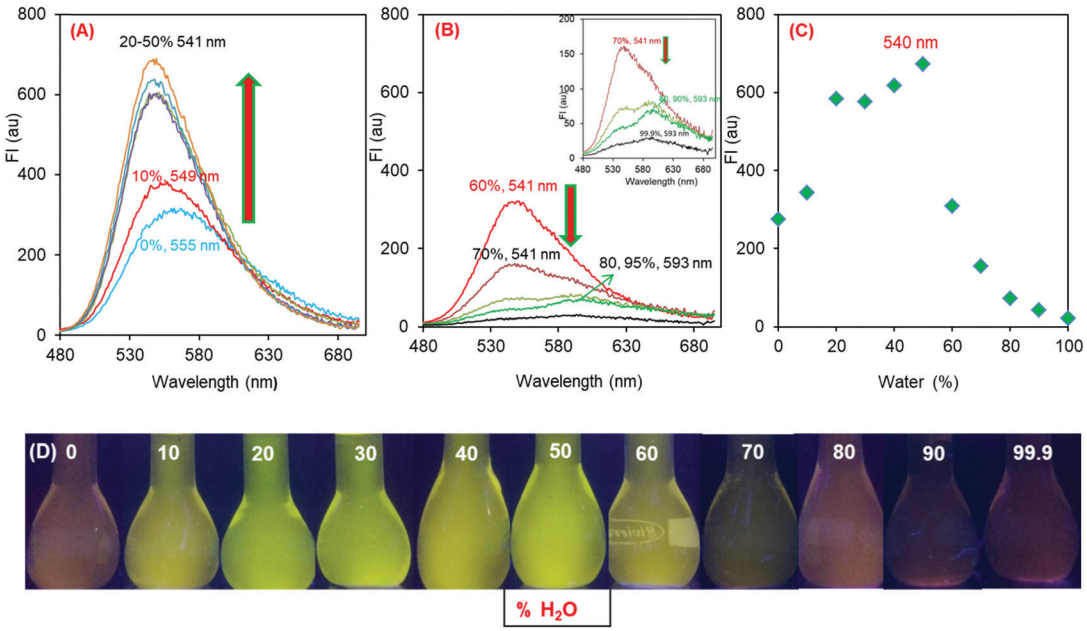

Fig. 3 (A and B) The fluorescence spectra of **HPBI** (5 μM) in CH_3CN–H_2O binary mixtures; (C) plot of fluorescence intensity against water (%); (D) the fluorescence color of the solutions of **HPBI** (5 μM) in CH_3CN–H_2O binary mixtures.

fluorescence intensity as the concentration of **HPBI** changed from 5 (μM) to 50 (μM) in CH_3CN–H_2O (1 : 1) mixture. Later, **HPBI** (50 μM) in CH_3CN–H_2O (1 : 1) was used for the development of LFPs on multiple surfaces.

3.4 Morphological studies of HPBI in CH_3CN–H_2O (1 : 1) mixture

The development of LFPs is considerably controlled by the size of the fluorescent aggregates of the material. In order to understand the aggregation state of **HPBI** in CH_3CN–H_2O (1 : 1), dynamic light scattering, fluorescence microscopic, FE-scanning electron microscopic, and TEM images were recorded. The recording of DLS of **HPBI** (50 μM) stated the formation of nano-aggregates with a hydrodynamic diameter of nearly 100 nm (Fig. 4A). The SEM and TEM studies (Fig. 4B–C) on the thin film of the same solution also displayed the formation of nano-aggregates with 50–100 nm size. On observing this solution under a fluorescence microscope, green fluorescent particles were observed. The formation of the nano-aggregates was further confirmed by the Tyndall effect (ESI,† Fig. S10). All these studies are in consonance with each other and confirm the spherical nano-aggregates of **HPBI** in the CH_3CN–H_2O (1 : 1) mixture.

3.5 Development of latent fingerprints

In order to check the versatility of nano-aggregates of **HPBI** (50 μM, CH_3CN–H_2O 1 : 1) for developing latent fingerprints, the fluorescence imaging of LFPs was performed on both non-porous surfaces such as aluminium foil, glass, steel plate, coin, and translucent paper as well as porous surfaces such as paper currency, brick, and filter paper. The LFPs were initially obtained by softly pressing the thumb on the desired surface. The solution of **HPBI** nano-aggregates (approx. 0.5 mL) was sprayed on the surface and within 30 seconds, green or yellow green (depending on the nature of the surface) fluorescent fingerprint appeared under illumination of a 365 nm lamp (Fig. 5A–J). This spray method, in general, is most versatile as it can be easily applied to a large surface area and is not restricted by the size and shape of the substrate. It was found that the fingerprints on different surfaces were clearly visible to naked eyes with high contrast and resolution, and did not require any post treatment. Compared with other surfaces, the LFPs on wood (natural) and plywood (synthetic) were less resolved, probably due to the penetration of the solution in wood and the dark background of plywood. The washing of the developed fingerprints with water did not affect their resolution. Quite inevitably, the hydrophobic green fluorescent spherical nano-aggregates of **HPBI** did not dissolve in water and preferentially stuck on to the ridges and were not spread on the furrows. As a result, the ridges appeared green fluorescent with the furrows remaining non-fluorescent. This selective interaction of the **HPBI** nano-aggregates with the ridges can be attributed to the hydrophobic and electrostatic interactions of the **HPBI** nano-aggregates with components of sebum and electrolytes in the sweat of fingerprints. The hydrophobicity of **HPBI** is due to a number of phenyl groups and the electrostatic interactions arise due to the dipole interactions of carbon–heteroatom bonds with polar compounds deposited from sweat. However, it may not be possible to distinctly differentiate the contribution of hydrophobic and electrostatic interactions.

We were able to develop latent fingerprints with distinct level 1–3 details without any post treatment (thermal or chemical). Latent fingerprints are classified into three types based on the level of information they provide. All the levels of information were obtained upon the magnification of one of the developed fingerprints. This representative example can be seen in Fig. 5K for the level 1 and level 2 details. The magnified images of these regions have been represented as core (level 1, Fig. 5O), small and ridge end (Fig. 5L and M), bifurcation, ridge dot, island, lake (level 2, Fig. 5N, P, Q and R), and sweat pores (level 3, Fig. 5S). Even, beyond this, the pores could be differentiated as open pores, closed pores, rounded pores, or pear-shaped pores in different sections of the fingerprint (Fig. 5T–W). These level 3 details are unique and are extremely important in the identification of LFPs, especially if LFPs are in partially damaged state.[27–29] Hence, **HPBI** nano-aggregates can be used to provide the *prima facie* clear evidence to prove the identity of an individual with minimum efforts and clarity. All the images were taken by a Canon 77D camera.

The aging of fingerprints is usually associated with the change in the sebaceous material present in the fingerprint residue. The LFPS can undergo loss of water due to the evaporation and decomposition of organic molecules such as saturated and unsaturated fatty acids and squalene, and it may be difficult to develop fingerprints after a long duration from their deposition due to a loss of selective interactions between

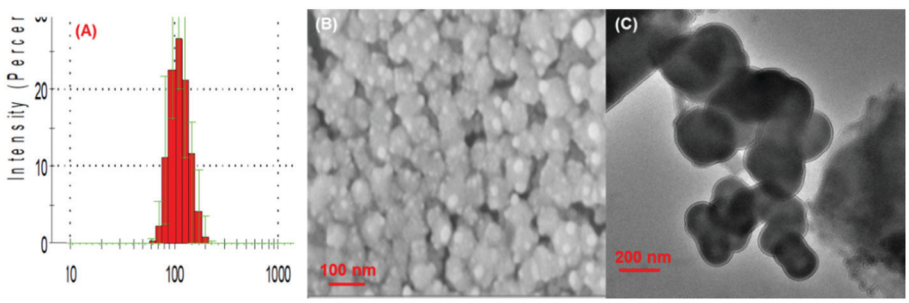

Fig. 4 (A) DLS studies, (B) SEM, and (C) TEM images of **HPBI** (50 μM) in CH_3CN–H_2O (1 : 1).

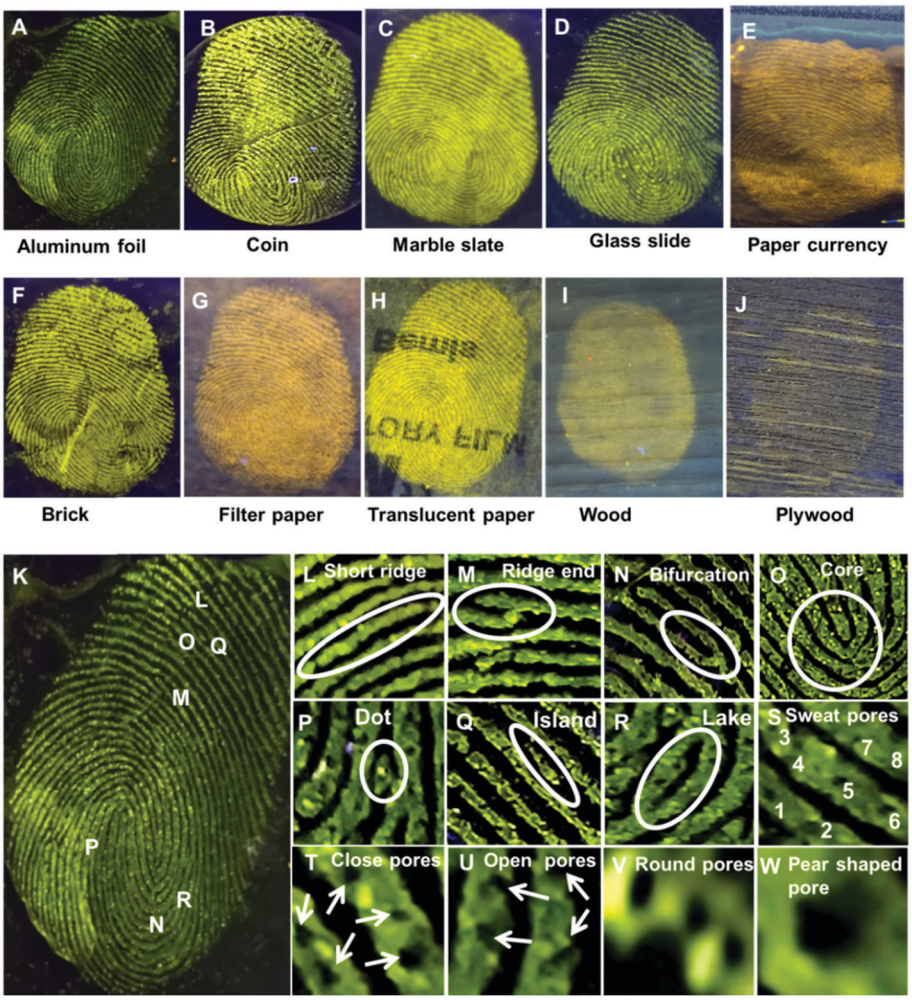

Fig. 5 (A–J) The latent fingerprints developed on various surfaces such as aluminium foil, coin, marble slate, glass slide, paper currency, brick, filter paper, translucent paper, wood, and plywood; (K) LFP A enlarged; (L–R) level 2 identifications as short ridge, ridge end, bifurcation, core, dot, island, and lake represented on K, and enlarged ones as separate squares; Level 3 details (S) Sweat pores; (T) Closed pore; (U) open pore; (V and W) shape of the pore.

the fluorescent material and the residues present in the ridges. The fingerprints encountered in crime scenes are often aged rather than freshly deposited; thus, aging presents a significant challenging task for latent fingerprint detection. In order to determine the ability of **HPBI** nano-aggregates in developing aged fingerprints, the fingerprints were kept on the shelf in the lab and were developed after defined time periods. Fig. S11 (ESI†) clearly shows the finely resolved ridge details of fingerprints as old as 10 days without loss in the resolution.

For finding the real-life application of nano-aggregates of **HPBI** to develop fingerprints, a piece of porous brick was lifted by a person using three fingers (index, middle, and ring fingers) on one surface of the brick and thumb on the opposite surface and was placed on the working shelf. The surface with three fingers (Fig. 6A) was sprayed with a solution of **HPBI** nano-aggregates. Quite interestingly, within a few seconds, the solvent was soaked by the brick material and clear fingerprints of the three fingers appeared on the surface under illumination of 365 nm light (Fig. 6B). The magnified images of these fingers (Fig. 6C) display clearly visible ridges and furrows of all the three fingers, and level 2 and level 3 details can be collected by the super-resolution of these impressions under camera. However, some parts of the fingerprints are not very clear either due to the non-planar surface of the brick and at some parts due to the over deposition of the **HPBI** nano-aggregates.

Furthermore, these fluorescent LFP images were collected on commercially available cello tape. After removing the cello tape from the developed fingerprint area, although the fluorescent intensity on the cello tape was decreased (Fig. 6D and E), the resolution of the fingerprint was not adversely affected and there was no loss of information. The fingerprint on the cello tape remained clear even after a week. Therefore, the collection of fluorescent fingerprints on cello tape provides an efficient and clean method for transporting fingerprints by the forensic investigating team to the forensic lab.

3.6 FE-SEM and fluorescence microscopic imaging of LFP

FE-SEM and fluorescence imaging were performed after the latent fingerprints were developed on a glass surface. The FE-SEM image captured at a magnification of 100× displayed

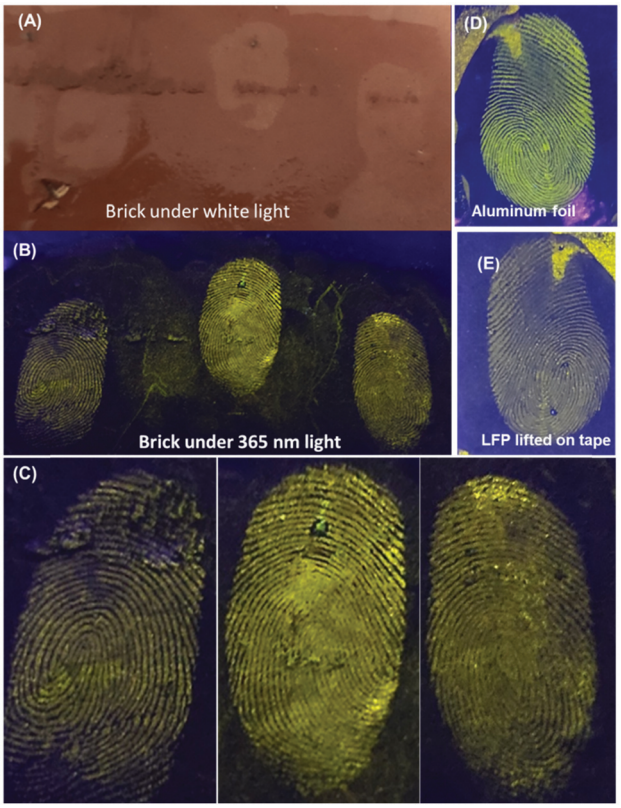

Fig. 6 (A) Day light illumination of LFPs of three fingers while clutching the brick. (B) LFPs on the brick illuminated under 365 nm light. (C) Enlargement of the image (B). (D) The LFP developed on an aluminium foil. (E) The LFP(D) lifted on cello tape.

the selective adhesion of HBPI on to the ridges (Fig. 7A) and the furrows remain unfilled. The surface of ridge was further analyzed at 200k× to reveal the filling of the ridge with spherical particles (Fig. 7B). The fluorescence microscopic image of LFP recorded in green channel (on excitation by blue light) also revealed the selective adhesion of nano-aggregates of **HPBI** on the ridges, as evident from the green fluorescence (Fig. 7C) and could be easily differentiated from the non-fluorescent furrows. One can clearly see the sweat pores pattern embedded in the ridges, which appear non-fluorescent (Fig. 7C).

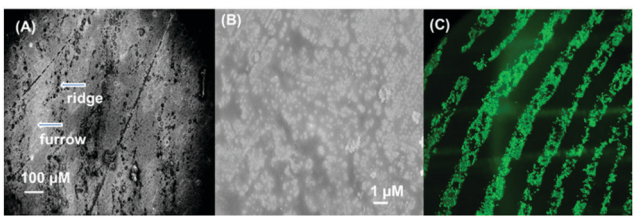

Fig. 7 (A) FESEM image of the developed LFP at 100× displaying the selective adhesion of **HPBI** on the ridges and hollow furrows; (B) the shape of particles on the ridge when magnified at 200k×; (C) image of the latent fingerprint displaying bright green fluorescent ridges embedded with non-fluorescent sweat pores.

4. Conclusions

We have synthesized double ESIPT and AIE-based fluorescent organic molecule **HPBI** for the efficient (<2 minutes) fluorescence imaging of LFPs on various surfaces such as aluminium foil, currency paper, marble tile, glass and steel surfaces, and translucent paper. DLS studies, SEM, and TEM images confirmed the aggregation of the **HPBI** molecules into highly fluorescent spherical nano-aggregates with 50–100 nm size. The nano-aggregates of **HPBI** filled the ridges due to hydrophobic and electrostatic interactions between the nano-aggregates and the components of the fingerprint ridges. LFPs clearly revealed level-2 details such as the ridge ending, islands, and bifurcation, as well as level-3 details such as ridges path deviation, edge contours, and sweat pores with high contrast and no background interference. Even, beyond this, the pores could be differentiated as open pores, closed pores, rounded pores, or pear-shaped pores in different sections of the fingerprint. These level 3 details are unique and are extremely important in the identification of LFPs, especially if the LFPs are in a partially damaged state. The development of aged LFPs and their lifting on cello tape without any abrasion are significant features for the transport of latent fingerprints from the crime scene to the forensic laboratory.

Author contributions

Manzoor Ahmad – execution of all experimental work, Gulshan Kumar and Vijay Luxami – theoratical work. Satwinderjeet Kaur – fluorescence recording of LFPs. Prabhpreet Singh – drafting and editing manuscript. Subodh Kumar – Conceptualization, drafting manuscript and raising funds.

Conflicts of interest

There are no conflicts of interest to declare.

Acknowledgements

This work was supported by Department of Science and Technology, New Delhi, SERB grant EMR/2016/001535. We thank UGC for UPE and PURSE programmes to the university and DST for FIST program. SK thanks UGC for UGC-BSR faculty F.4-5(11)/2019 (BSR) fellowship.

References

1 R. Saferstein, *Criminalistics: An Introduction to Forensic Science*, Prentice Hall, Englewood Cliffs, NJ, 9th edn, 2006.
2 C. Champod, C. Lennard, P. Margot and M. Stoilovic, *Fingerprints and Other Ridges Skin Impressions*, CRC Press, Boca Raton, FL 2004.
3 C. Champod and P. Chamberlain, in *Handbook of Forensic Science*, ed. J. Fraser and R. Williams, Willan Publishing, Cullompton, UK, 2009, pp. 57–83.

4 A. R. W. Jackson and J. M. Jackson, *Forensic Science*, Prentice Hall, Harlow, England, 2nd edn, 2008.
5 H. Faulds, *Nature*, 1880, **22**, 605.
6 D. Maltoni, D. Maio, A. Jain and S. Prabhakar, *Handbook of Fingerprint Recognition*, Springer-Verlag, New York, 2003.
7 A. Becue, *Anal. Methods*, 2016, **8**, 7983–8003.
8 M. Wang, M. Li, A. Yu, Y. Zhu, M. Yang and C. Mao, *Adv. Funct. Mater.*, 2017, **27**, 1606243.
9 A. Baride, G. Sigdel, W. M. Cross, J. J. Kellar and P. S. May, *ACS Appl. Nano Mater.*, 2019, **2**, 4518–4527.
10 Z. Wang, X. Jiang, W. Liu, G. Lu and X. Huang, *Sci. China Chem.*, 2019, **62**, 889–896.
11 L. Cai, M. C. Xia, Z. Wang, Y. B. Zhao, Z. Li, S. Zhang and X. Zhang, Chemical Visualization of Sweat Pores in Fingerprints Using GO Enhanced TOF-SIMS, *Anal. Chem.*, 2017, **89**, 8372–8376.
12 B. Su, *Anal. Bioanal. Chem.*, 2016, **408**, 2781–2791.
13 X. Ran, Z. Wang, Z. Zhang, F. Pu, J. Ren and X. Qu, *Chem. Commun.*, 2016, **52**, 557–560.
14 J. Kopka, M. Leder, S. M. Jaureguiberry, G. Brem and G. O. Boselli, *J. Forensic Sci.*, 2011, **56**, 1235–1240.
15 P. Hazarika and D. A. Russell, *Angew. Chem., Int. Ed.*, 2012, **51**, 3524–3531.
16 A. H. Malik, A. Kalita and P. K. Iyer, *ACS Appl. Mater. Interfaces*, 2017, **9**, 37501–37508.
17 J. H. Yoon, Y. J. Jin, T. Sakaguchi and G. Kwak, *ACS Appl. Mater. Interfaces*, 2016, **8**, 24025–24029.
18 H. Chen, R. L. Ma, Y. Chen and L.-J. Fan, *ACS Appl. Mater. Interfaces*, 2017, **9**, 4908–4915.
19 L. Xu, Y. Li, S. Li, R. Hu, A. Qin, B. Z. Tang and B. Su, *Analyst*, 2014, **139**, 2332–2335.
20 Y. Li, L. Xu and B. Su, *Chem. Commun.*, 2012, **48**, 4109–4111.
21 (*a*) P. Singh, H. Singh, R. Sharma, G. Bhargava and S. Kumar, *J. Mater. Chem. C*, 2016, **4**, 11180–11189; (*b*) S. Dhiman, M. Ahmad, G. Kumar, V. Luxami, P. Singh and S. Kumar, *J. Mater. Chem. C*, 2021, **9**, 1097–1106.
22 K. Kumar, H. Singh, V. Vanita, R. Singh, K. B. Joshi, G. Bhargava, S. Kumar and P. Singh, *Sens. Actuators, B*, 2019, **283**, 651–658.
23 Z. Qiu, B. Hao, X. Gu, Z. Wang, N. Xie, J. W. Y. Lam, H. Hao and B. Z. Tang, *Sci. China Chem.*, 2018, **61**, 966–970.
24 R. Suresh, S. K. Thiyagarajan and P. Ramamurthy, *Sens. Actuators, B*, 2018, **258**, 184–192.
25 L. Xu, Y. Li, S. Wu, X. Liu and B. Su, *Angew. Chem., Int. Ed.*, 2012, **51**, 8068–8072.
26 Y. Li, L. Xu, Y. He and B. Su, *Electrochem. Commun.*, 2013, **33**, 92–95.
27 S. Hu, Z. Cao, L. Zhou, R. Ma and B. Su, *J. Electroanal. Chem.*, 2020, **870**, 114238.
28 Y. He, L. Xu, Y. Zhu, Q. Wei, M. Zhang and B. Su, *Angew. Chem., Int. Ed.*, 2014, **53**, 12609–12612.
29 M. Zhang, A. Becue, M. Prudent, C. Champod and H. H. Girault, *Chem. Commun.*, 2007, 3948–3950.
30 H. Chen, R. L. Ma, Z. Fan, Y. Chen, Z. Wang and L. J. Fan, *J. Colloid Interface Sci.*, 2018, **528**, 200–207.
31 J. C. Duff and E. J. Bills, *J. Chem. Soc.*, 1932, 1987–1988.
32 E. N. Djuidjea, S. Sciabicab, R. Buzzia, V. Dissettea, J. Balzarinic, S. Liekensc, E. Serraae, E. Andreottid, S. Manfredinia, S. Vertuania and A. Baldisserotto, *Bioorg. Chem.*, 2010, **101**, 103960.
33 Y. L. A. Kwok, J. Gralton and M. L. McLaws, *Am. J. Infection Control*, 2015, **43**, 112–114.
34 J. Rahman, J. Mumin and B. Fakhruddin, *Annals of Global Health*, 2020, **86**, 75.
35 S. M. Mueller, S. Martin and M. Grunwald, *PLoS One*, 2019, **14**, e0213677.
36 M. M. Montoya and R. A. J. Janssen, *Adv. Funct. Mater.*, 2017, **27**, 1605779.